Journal of Power Sources 403 (2018) 192–198

Contents lists available at ScienceDirect

Journal of Power Sources

journal homepage: www.elsevier.com/locate/jpowsour

Woven gas diffusion layers for polymer electrolyte membrane fuel cells: Liquid water transport and conductivity trade-offs

S. Hasanpour[a,b,d], M. Ahadi[c], M. Bahrami[c], N. Djilali[b,**], M. Akbari[a,d,*]

[a] Laboratory for Innovations in Microengineering (LiME), Department of Mechanical Engineering, University of Victoria, Victoria, BC, V8P 5C2, Canada
[b] Department of Mechanical Engineering and Institute for Integrated Energy System, University of Victoria, Victoria, BC, V8W 3P6, Canada
[c] Laboratory for Alternative Energy Conversion (LAEC), School of Mechatronic Systems Engineering, Simon Fraser University, Surrey, BC, V3T 0A3, Canada
[d] Center for Advanced Materials and Related Technologies (CAMTEC), University of Victoria, Victoria, BC, V8P 5C2, Canada

HIGHLIGHTS

- Effect of different FEP loading on water breakthrough is investigated for woven GDLs.
- Water transport of woven GDLs was visualized employing fluorescent microscopy.
- The optimum FEP coating for thermal conductivity is 30 wt% among samples (0 and 55).
- Water propagate in treated GDLs and the breakthrough happens in compressed regions.

GRAPHICAL ABSTRACT

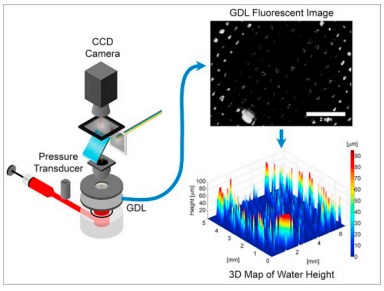

ARTICLE INFO

Keywords:
Woven gas diffusion layers
Water breakthrough
Fluorescent microscopy
Thermal conductivity
Electrical conductivity

ABSTRACT

Gas diffusion layers (GDLs) provide pathways for water removal in a polymer electrolyte membrane (PEM) Fuel Cell. Woven GDLs, have shown higher capability to retain water and improve performance under humid conditions compared to non-woven GDLs. In this work, we investigate water transport, distribution and location of breakthrough in woven GDLs using fluorescent microscopy. GDLs with no coating, 30, and 55 wt% fluorinate ethylene propylene (FEP) were investigated. FEP increases hydrophobicity and affects thermal and electrical conductivities. The results show that the FEP-treated GDLs have higher breakthrough pressures and water contact angles than non-treated GDLs. For untreated samples, water breakthrough occurs in non-compressed regions; whereas, for FEP-treated samples emergence occurs in the compressed regions. Furthermore, water was observed to first cover visible pores inside the GDLs prior to breakthrough. Increasing FEP loading promotes the propagation of water inside the GDLs. Thermal conductivity is found to improve with FEP coating and attains a maximum at 30 wt% FEP loading, whereas electrical conductivity decreases with increasing FEP loading. This analysis shows more pores are engaged in water transport with higher FEP loading. Implementation of woven GDLs in fuel cell design requires a balancing of the water and heat transport benefits with the reduced electrical conductivity.

* Corresponding author. Center for Advanced Materials and Related Technologies (CAMTEC), University of Victoria, Victoria, BC, V8P 5C2, Canada.
** Corresponding author.
E-mail addresses: ndjilali@uvic.ca (N. Djilali), makbari@uvic.ca (M. Akbari).

https://doi.org/10.1016/j.jpowsour.2018.09.076
Received 21 May 2018; Received in revised form 10 August 2018; Accepted 21 September 2018
Available online 09 October 2018
0378-7753/

1. Introduction

The gas diffusion layer (GDL) plays a central role in the performance of polymer electrolyte membrane fuel cells (PEMFCs) [1]. The GDL facilitates transport of reactants from the flow channels to the catalyst layer and contributes to the transport of electrons and heat from the membrane electrode assembly (MEA), where the electrochemical reactions occur. Additionally, the GDL helps control the level of moisture in a fuel cell. Proper water management ensures that by-product water is removed from the catalyst layer to prevent flooding while maintaining the catalyst layer and MEA hydrated at the same time [2].

The GDL is a porous structure that is fabricated either by weaving carbon fibers into a carbon cloth or randomly distributing carbon fibers to form a non-woven carbon paper. Carbon fibers are mostly made of polyacrylonitrile (PAN) using a solvent spinning process [1]. Spun PAN yarns, used to make carbon cloth, are produced through the Worsted process, where yarns are generated and wrapped around a bobbin for weaving. The woven carbon fiber is then carbonized at a minimum temperature of 1600 °C (often under vacuum) [1]. This manufacturing process leads to a more flexible GDL structure. Non-woven GDLs are manufactured using the papermaking technology followed by sintering [1]. This process leads to a different microstructure for the non-woven GDLs than their woven counterparts. The pore sizes in woven GDLs vary in a wide range from 2 to 100 μm, whereas pore sizes in non-woven GDLs range from 10 to 30 μm. The wide range of pore size distribution in the woven GDLs is due to the multiscale microstructure of the constituent yarns that are formed from packed fine fibrils with large pores located between the yarns [3,4]. Moreover, woven GDLs have lower porosity and less tortuous structure compared to non-woven GDLs [3]. In addition, the in-plane porosity distribution in woven GDLs has a sinusoidal shape, which varies between 80 and 90%, whereas non-woven GDLs porosity distribution is more random. GDLs are commonly treated with hydrophobic polymers such as polytetrafluoroethylene (PTFE) or fluorinated ethylene propylene (FEP) [5] to improve the hydrophobicity of the GDLs using dipping, spraying, or brushing methods. Another process that improves the performance of the GDL is applying a thin microporous layer (MPL), to the side which is in contact with the catalyst layer (CL), to facilitate the wicking of liquid water from the CL to the GDL. MPLs have a pore size distribution much smaller than GDLs, from ~100 to 500 nm [6].

Experimental studies to characterize GDLs have been conducted (1) to understand transport properties, such as permeability, diffusivity, breakthrough pressure, electrical conductivity and thermal conductivity; and (2) to analyze the microstructure, including bulk porosity, pore size distribution, and porosity distribution. One of the key properties of GDLs is water breakthrough. Breakthrough analysis [7–10] provides information about the required pressure to overcome the capillary force and also the location of the water breakthrough in GDLs. Benziger et al. [7] investigated water breakthrough pressure for woven and non-woven GDLs without an MPL and showed that woven GDLs have a lower breakthrough pressure (~2 kPa) compared to non-woven GDLs (Toray samples ~7 kPa). The lower breakthrough pressure of woven samples is due to larger pores located between yarns of the woven GDLs. Furthermore, increasing the PTFE loading of the GDL slightly increases the breakthrough pressure. Lu et al. [9] investigated non-woven GDLs with and without MPL (SGL 25BA and SGL 25BC). SGL samples are more porous compared to Toray samples and have larger pores and porosity values [11]. A breakthrough pressure of 1.7 kPa was reported for GDLs without MPL and 6.7 kPa for GDLs with MPL [9]. This is due to the smaller pores of the MPL, which are expected to increase the breakthrough pressure.

Visualization of water breakthrough in GDLs has been studied with different imaging techniques. Two main techniques are X-ray microcomputed tomography (X-μCT) and fluorescent microscopy [12]. Flückiger et al. [10] performed X-μCT imaging of water breakthrough on non-woven GDLs to observe their water content. The scan time was as low as 5 min with a sample size of 2.5 mm in diameter. This study showed the saturation curve for different water intrusion pressures. More recently, Weber et al. [13] designed a new test setup to replicate the land and channel in the flow field and observe the water saturation in GDLs. The scan time was about 8 min with a sample size of 3.2 mm in diameter. Although X-μCT provides high spatial resolution and allows characterization of GDLs and interfaces in MEAs, the small sample size and the low temporal resolution limit the breakthrough analysis [11,14]. However, in the recent 3D X-μCT study of Eller et al. [15] resolution was improved with scan times of 3.2 s and 1% false water detection. Nonetheless, fluorescent microscopy temporal and spatial resolutions currently allow better tracking of the emergence of water. The challenges with optical fluorescent microscopy are the depth of field, which does not allow observation of the whole structure of GDLs, and the need for modified sample holders to provide access of light to the GDLs structure [16]. Litster et al. [16] visualized water transport through the thickness of non-woven GDLs and found the location of the breakthrough on the surface. Bazylak et al. [2] investigated the effect of compression on the location of the breakthrough in non-woven GDLs and showed that compression damages the PTFE and fiber structure and creates preferential pathways for water removal in the compressed areas.

Previous studies mainly characterized non-woven GDLs. However, a comprehensive study to understand water transport in woven GDLs is warranted since these GDLs have a higher capacity to retain water compared to non-woven GDLs (cf. [17]). The present study aims to investigate water transport in woven GDLs at the microstructure level. For this purpose, carbon cloth GDLs with three different FEP loadings (0, 30 and 55 wt%) were used to visualize water transport. The study reveals why woven GDLs have a higher capacity to keep water inside compared to non-woven GDLs, and documents the associated changes in thermal and electrical conductivity.

2. Experimental

2.1. GDL

In this study, a woven GDL, Avcarb 1071 HCB (from Fuelcell Earth), was used. This woven GDL has a thickness of 350 μm and porosity of 65 %. FEP solution (Teflon FEPD 121 Fluoroploymer Dispersion) was used to treat the AvCarb GDLs with 30 and 55 wt% FEP loadings. GDLs were dipped into the solution for 1 min and then placed on needle-point holders. The holders were kept in the vacuum oven at room temperature for an hour; the temperature was then increased to 100 °C for one additional hour. This process allowed evaporation of water and other solvents from the GDLs. To evaporate the surfactant, the GDLs were kept in a muffle oven for 50 min while the oven temperature was ramping up to reach 260 °C, and then for an additional 10 min at a constant 260 °C. To sinter the polymer, the temperature was ramped up to 280 °C over 20 min and kept at 280 °C for 20 min (also see Ref. [5]).

2.2. Visualization and breakthrough pressure

The apparatus to measure the breakthrough pressure and perform fluorescence microscopy to visualize water transport is described below. A dilute water solution of 1 mM rhodamine B (excitation: emission 540 nm: 625 nm) was prepared to trace water transport in the plane of the GDLs. Since this solution was dilute, dying the water had negligible effect on the properties of water (compared to pure water).

2.2.1. Apparatus

Samples were placed in an assembly and water was injected with a syringe pump at a rate of 0.02 ml min^{-1}. The clamping device has a top plate made from Plexiglas to visualize water, and it has a small hole (with diameter of 5 mm) for water removal. The O-ring diameter is 9 mm and the area between O-ring and open hole is under pressure. The

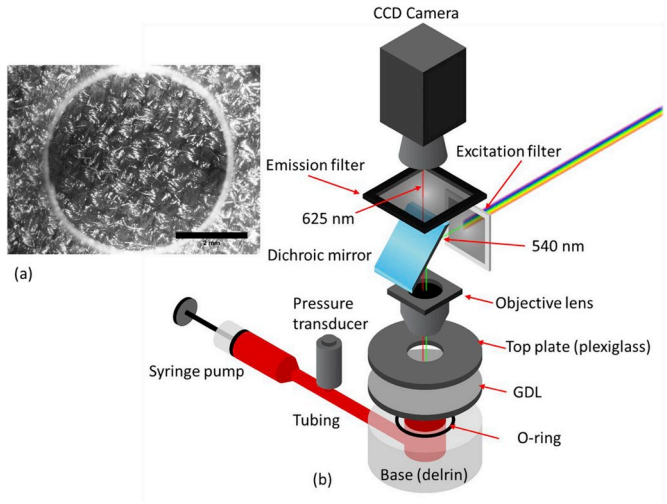

Fig. 1. (a) Black and white image of woven GDL (scale bar is 2 mm) (b) Schematic of the fluorescent microscopy of GDL.

test performed under isothermal room temperature conditions. An upright fluorescent microscope (DP 73 Olympus BX51), with CY3 filter and 2× objective having a numerical aperture of 0.06, was used in this experiment. A schematic of the clamping device and microscope is shown in Fig. 1. Images were all taken in black and white. The sample was illuminated with fiber optic, Fig. 1(a). The acquisition software was Olympus CellSense. Water pressure was measured with a differential pressure transducer (Honeywell FP2000) connected to a data acquisition system.

2.2.2. Image and data acquisition

A cooled CCD (charge-coupled device) camera was used to capture the transient transport of water. The nominal depth of the field, calculated from $d_{field} = \lambda/NA^2$, was found to be 150 µm, allowing signals to reveal inside the porous structure. The depth of field of view for the sample was 100 µm that could cover 7–8 fibers as well as the space where the water flowed. Intensity of the 8-bit images could be correlated to the height of the water on the surface, using the following formula [16]:

$$\eta = \frac{100\mu m}{255} I \tag{1}$$

where η is the observable height and I is the intensity of the image. The field of view was 6.5 mm × 5 mm with a spatial resolution of 4.6 µm, and images were acquired at 20 frames per second. This field of view was large enough to cover many pores (~2–100 µm [4]) on the surface. Scanning electron microscopy (SEM; Hitachi S−3500N) and energy dispersive X-ray spectroscopy (EDS; Hitachi S−3500N) were employed to observe microstructure of GDLs with different FEP loadings, and also to deduce distribution of FEP in the GDLs.

2.3. Thickness measurement

The thickness of the GDL samples were measured at different pressures using a custom-made testbed (Thickness Under Compression-Resistivity Under Compression, or TUC_RUC) and protocol described in detail in Ref. [18].

2.4. Thermal conductivity measurement

Thermal conductivities were measured using a guarded heat flux (GHF) testbed, which was custom-made based on ASTM Standard E1530-11 and described in detail in Refs. [18–20]. The procedure for measuring bulk thermal conductivity relies on the measurement of thermal resistances of at least two material samples with different thicknesses and then deconvoluting the bulk and contact thermal resistances by subtracting the two resistances as follows:

$$k_b = \frac{t_2 - t_1}{(R_2 - R_1)\,A} \tag{2}$$

where R_1 and R_2 are the resistances measured inside the testbed; k_b is the bulk conductivity of the sample, and t_1 and t_2 are the thicknesses of the measured sample. In this study, since only one thickness of GDL was available, different thicknesses were simply made by stacking the material. It should be noted that the total thermal resistance measured by the GHF testbed consists of the bulk resistance and *two* thermal contact resistances (TCRs) between a sample and the apparatus (the GHF fluxmeters). However, in a stack of several samples, there is an additional TCR between the samples in contact with each other. Therefore, when subtracting resistances of two stacks of samples ($R_2 - R_1$ in Eq. (2)), the two TCRs between the stacks and the apparatus (fluxmeters) cancel out, and only the difference in bulk resistances of the samples in the stacks and the TCRs between the samples remain. However, as also shown in Refs. [21–24], TCRs between GDLs in a stack of GDL samples are negligible compared to the bulk resistances of the samples. Therefore, the result of subtraction of resistances in Eq. (2) (i.e. $R_2 - R_1$) provides an accurate measure of the difference in bulk resistances of the samples in the stacks. This stacking method has been widely used in the literature for measuring different layers of fuel cells, including porous transport layers [21–24] and catalyst layers [25].

2.5. Electrical conductivity

Measurements of electrical conductivity were performed using a Micro Junior 2 micro ohmmeter (Raytech, USA) comprising four custom-made gold-plated probes. A sample was clamped between the probes, and a clamping pressure of 1500 kPa was applied on the probes. Similarly, to the GHF thermal resistance measurements, the electrical conductivity could be deconvoluted from measurements of at least two sample thicknesses using Eq. (2). Again, different thicknesses were made simply by stacking.

3. Results and discussion

The clamping device compressed the GDL under an O-ring at a pressure of 1.6 MPa (Sensor Products Inc.); see Fig. S2. This compression is within the range of compressions in actual fuel cell operation [2]. In-plane and through-plane SEM images of three different woven GDL samples, namely AvCarb 1071 HCB with 0, 30 and 55 wt% FEP loadings, are shown in Fig. 2. The images show that more FEP material is located on the surface than through the bulk structure of the GDLs. Increasing FEP loading changes the physical properties of the woven GDLs from flexible to more rigid. This may be due to filling the pores between fibers and yarns by FEP, which increases stiffness. The distribution of this polymer within the sample is important since an even distribution of FEP enhances the whole structure's hydrophobicity. The polymeric coating for the samples was investigated using EDS to map fluorine material on the surface and along the in-plane direction of the GDLs, and the resulting in-plane and through-plane distributions of fluorine and carbon are shown in Fig. 3(a) and (b), and the enhanced FEP content with higher loading is clearly illustrated, with a relatively even distribution through the two planes; we note that AvCarb without FEP shows trace amount of fluorine.

EDS analysis can also be used to quantify the material content. Table 1 shows weight percentage of each element in Fig. 3(a) (in-plane) and 3(b) (through-plane). There are errors associated for the weight percentage of fluorine and carbon on the surfaces and the cross sections. The trace amounts of fluorine in the non-treated samples is attributed to either noise or very small levels of contamination. Fluorine accumulates more on the surface, as indicated by the higher percentage

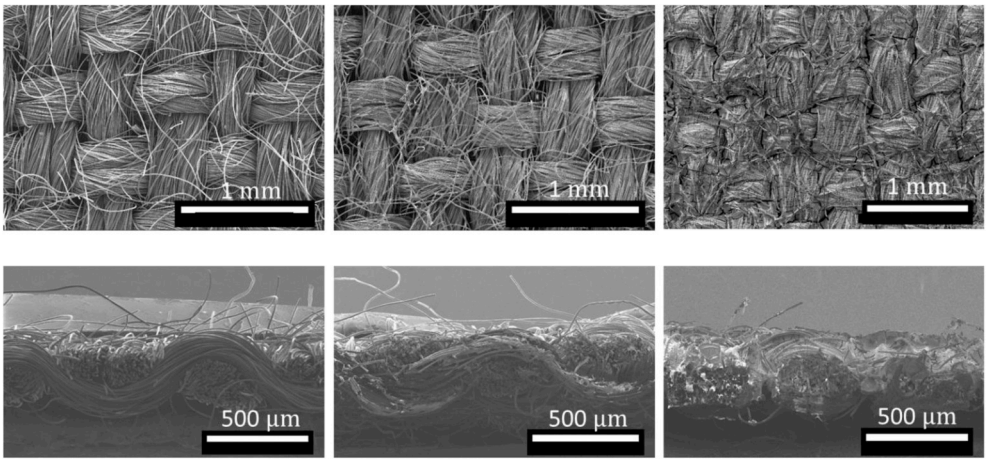

Fig. 2. SEM images of the in-plane and through-plane of GDLs for different FEP loading (0, 30 and 55 wt% FEP).

of fluorine in the in-plane direction than the through-plane direction. Similar results were reported for non-woven GDLs [26]. The higher content of hydrophobic polymer (PTFE or FEP) on the surface results in lower porosity near the surface for the treated GDLs.

The measured breakthrough pressures for the samples are shown in Fig. 4(a). Increasing FEP/hydrophobicity of the GDL can reduce the pore sizes and increase the contact angle, see Fig. 4(b); these factors in turn result in higher breakthrough pressure with higher FEP loading.

Visualizations at the starting time of the breakthrough and following breakthrough are monitored using fluorescent microscopy. Fig. 5 (a) shows the saturation curve over time, which was obtained by monitoring water emergence from the top plate of clamping device. The transient saturation curve shows the low amount of saturation before the breakthrough. However, after the breakthrough, the saturation increased significantly. For both cases, higher percentage of saturation was observed for modified GDLs compared to the pristine sample. Fig. 5(b) shows four instances of water transport in the woven GDLs. Water first filled the pores under the open window for all samples as the open window is located on the top of the injection hole. For the sample without coating, breakthrough occurred in the circular open window, and water covered the surface. However, samples with 30 and 55 wt% FEP followed a different scenario. Water first filled the pores in the circular window and then propagated to other pores in the in-plane direction of the GDLs; finally, breakthrough occurred in the compressed areas, with water covering the surface. The supplementary videos show water transport for GDLs with no coating (Movie S1), with 30 wt% FEP (Movier S2), 55 wt% FEP (Movie S3). Similar trend were observed when the test was performed on more samples (Fig. S1).

Supplementary video related to this article can be found at https://

Table 1
Carbon and fluorine percentage for 0, 30 and 55 wt% FEP loading GDLs.

Materials	In-plane [wt%]		Through-plane [wt%]	
	Carbon	Fluorine	Carbon	Fluorine
AvCarb 1071 – Without Coating	99.7	0.3	99.8	0.2
AvCarb 1071–30 wt% FEP	62.2	37.8	65.5	34.5
AvCarb 1071–55 wt% FEP	29.4	70.6	41.9	58.1

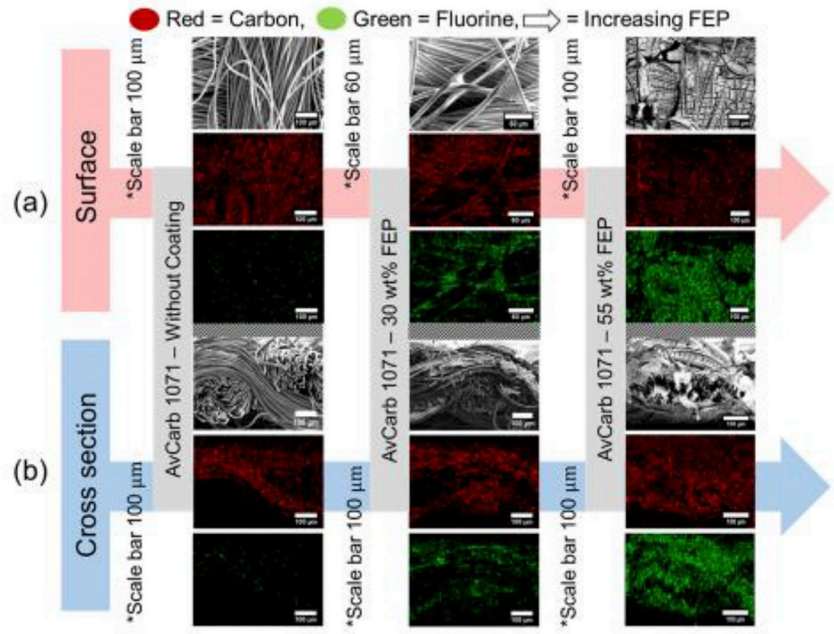

Fig. 3. EDS analysis mapping (a) in-plane distribution (b) through-plane of carbon (red) and fluorine (green) for different FEP loading sample (0, 30 and 55 wt%). (For interpretation of the references to colour in this figure legend, the reader is referred to the Web version of this article.)

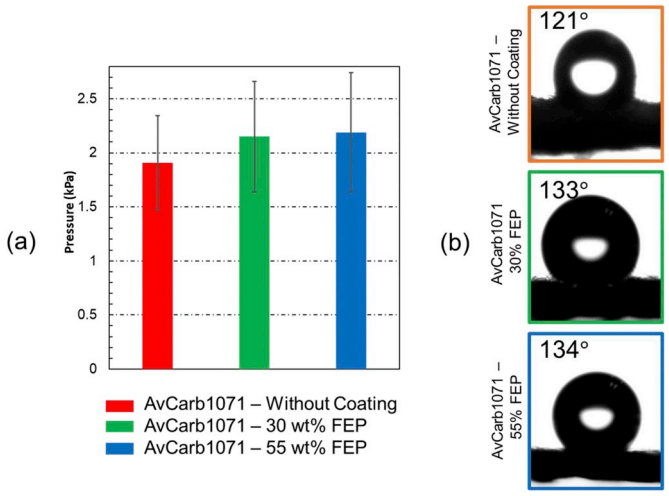

Fig. 4. (a) Breakthrough pressure and (b) water droplet contact angles of GDLs with different FEP loading (number of sample = 3).

doi.org/10.1016/j.jpowsour.2018.09.076.

The differences in water distribution patterns can be attributed to a number of factors. Water flow experiences higher resistance in the through-plane direction and will preferentially flow along lower resistance pathways. The lower in-plane resistant maybe because of the better pore connectivity and lower tortuosity, especially in the direction aligned with the strands, in the in-plane direction as compared to the through-plane. Higher hydrophobicity of the modified GDLs affects the breakthrough pressure and contact angles (Fig. 4). More hydrophobic pathways cause higher capillary pressures and enhanced water transport towards lower resistance regions. Another hindering factor for water transport in the through-plane direction is the accumulation of more FEP on the surface of GDLs, which causes smaller pores near the surface and requiring higher pressure to overcome this barrier. These factors would increase the resistance in the through-plane direction, and consequently, promote transport of water inside the GDL, filling of the pores first followed by break-throughs in the region under compression.

The intensity of the grayscale image can be correlated to the water height [17]. In Fig. 6(a), the circular shape is subtracted from the breakthrough image, and the corresponding water height distribution is illustrated in the 3D map. Emergence of water for the sample without coating occurs in the circular windows. However, for the FEP-loaded samples, water covers pores first in the areas under compression, and then emerges from the compressed regions. This is attributed to distortion of the GDL microstructure under compression. Compression can open some pathways for water in FEP-loaded woven GDLs, as was also shown for non-woven GDLs [2].

Fig. 7 illustrates through-plane water transport for untreated and treated GDLs. Water travels toward the open window and with no lateral movement in untreated samples; however, in the treated samples, water is forced to move laterally first and then emerges on the surface.

The variation of GDL thickness with compression is shown in Fig. 8(a) for samples with different FEP loadings; the error bars for these measurements are smaller than the data points and are not shown. The measurements show that the samples swell with increasing FEP treatment due to impregnation of fibers and the filling of gaps between fibers. Settling down of FEP material on the surfaces of the samples could also contribute to the increased thickness.

Thermal conductivity results, shown in Fig. 8(b), indicate that the 30 wt% FEP loading GDL has the optimum thermal conductivity. This is a direct result of impregnation of the samples by the FEP material, which has a higher thermal conductivity than air ($\sim 0.2\ W\ m^{-1}\ K^{-1}$ for FEP compared to the value of $0.02\ W\ m^{-1}\ K^{-1}$ for air). The optimal value is a result of the trade-off between the higher conductivity of FEP material with the increased thickness of the FEP-treated GDLs which lengthens the conduction path inside the samples. The through-plane thermal conductivity values measured in this study are in the same range as through-plane values reported in the literature for woven GDLs [22] ($\sim 0.28–0.32\ W\ m^{-1}\ K^{-1}$) and non-woven GDLs [27] ($\sim 0.15–2.1\ W\ m^{-1}\ K^{-1}$).

FEP loading has a significant impact on electrical conductivity as shown in Fig. 8(c). Whereas FEP provides better heat conduction pathways than air, it is an insulator for electric current, and the combination of impregnation of fibers, deposition of an insulating layer on the surface, and increased thickness result in a significant drop in electrical conductivity. Through-plane electrical conductivity data reported in literature are in the range of $\sim 250–2500\ S\ m^{-1}$ for non-woven GDLs [28–30].

4. Conclusion

Water transport, thermal conductivity, and electrical conductivity of woven GDLs with different FEP loadings were investigated in isothermal conditions at room temperature. Fluorescent microscopy visualization of water transport showed that for woven GDLs without FEP loading, water first fills bigger pores between yarns in the woven GDLs and then, breaks through a pore in the open area of the structure. FEP loaded-GDLs,

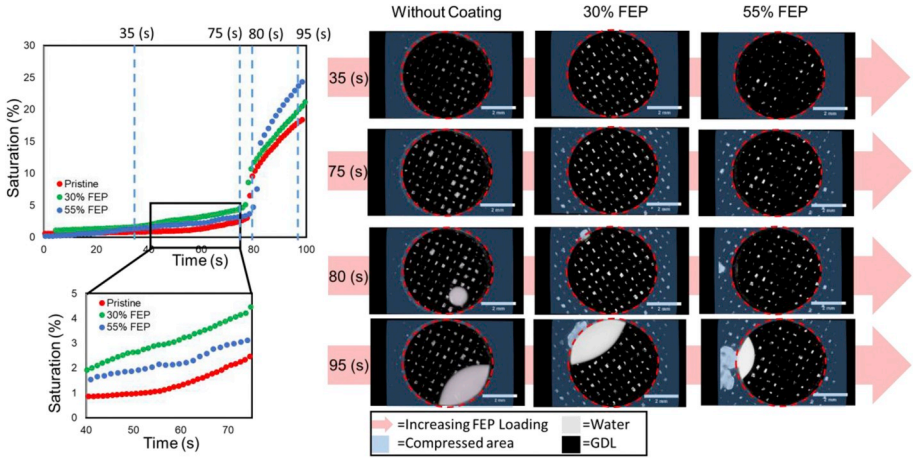

Fig. 5. (a) saturation over time (b) four instances of water saturation for GDLs without FEP, 30 and 55 wt% FEP (the scale bar is 2 mm).

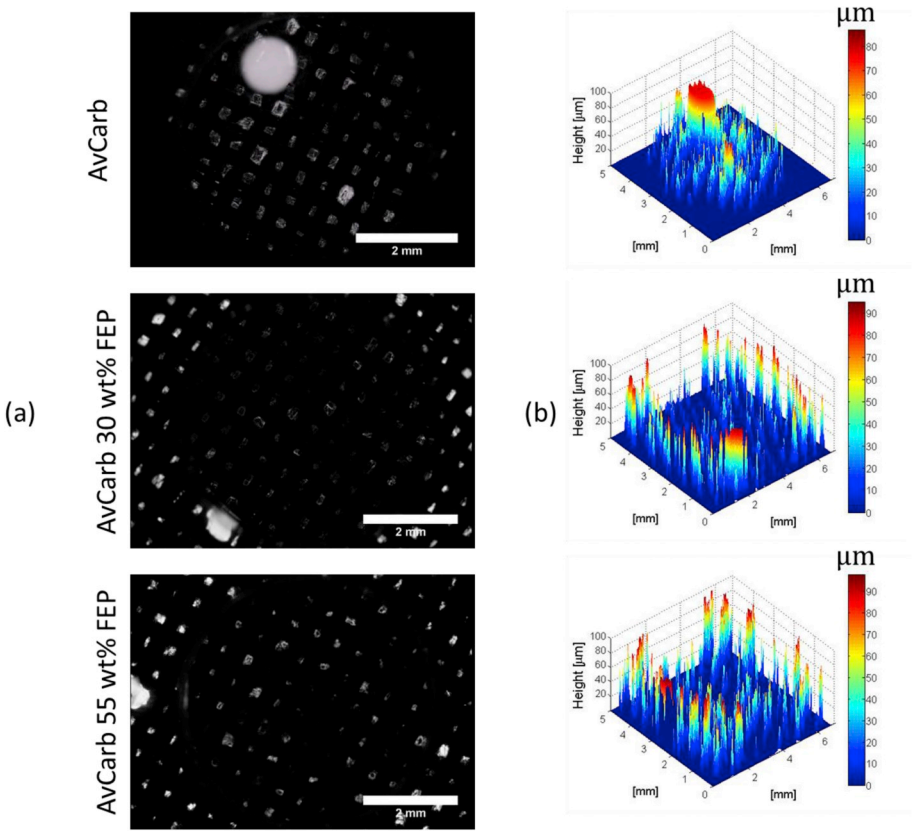

Fig. 6. (a) Fluorescent microscopy of the breakthrough location (scale bar is 2 mm) (b) 3D map of water height in GDL and breakthrough location on the surface.

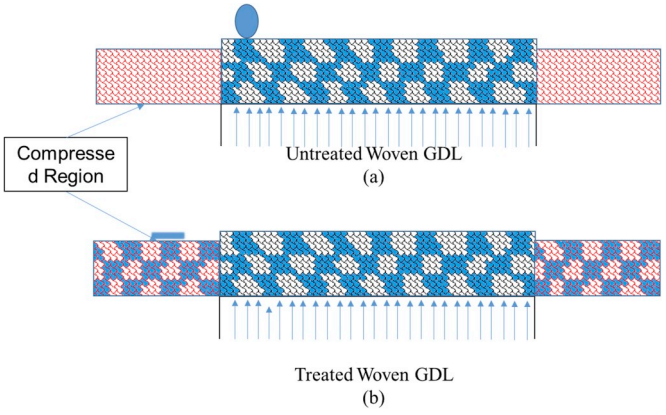

Fig. 7. Water transport inside of (a) untreated and (b) treated woven GDLs.

however, have higher breakthrough pressures due to smaller pores and higher hydrophobicity. As such, water flows more in the in-plane direction of the GDLs. Furthermore, the occurrence of the breakthrough is in the area under compression. As in the case of non-woven GDLs [2], water breakthrough is due to distortion of the fibers and FEP material under compression. Higher FEP loading results in the swelling of the GDL due to partial filling of pores, possibly impregnation of fibers, as well as coverage of the sample surfaces with FEP material. Thermal conductivity measurements showed the existence of an optimum FEP loading (near 30 wt%) as a result of a trade-off between the partial fillings of the pores and increased the thickness of the sample by FEP. On the other hand, electrical conductivity decreased monotonically and significantly with FEP loading. In implementing woven GDLs in fuel cells, FEP treatment needs to be carefully determined in terms of trade-offs between improved water transport, heat, and electrical conduction, possibly using multi-objective optimization [31,32].

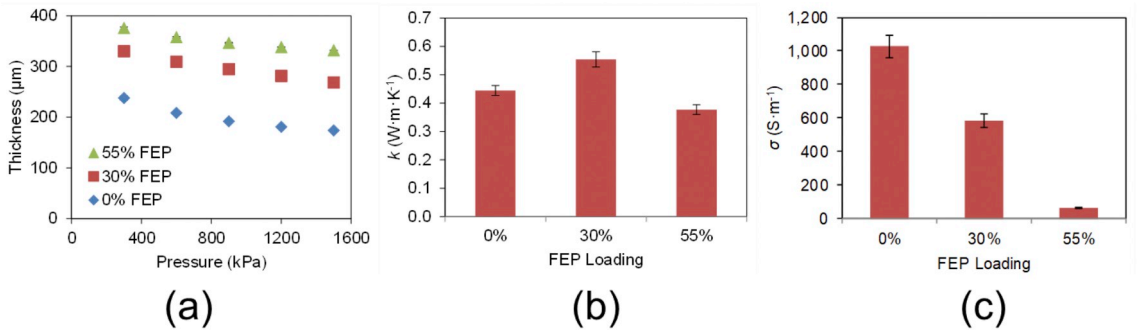

Fig. 8. (a) Thicknesses of GDL samples versus pressure, (b) Thermal conductivity and (c) Electrical Conductivity versus FEP loading (number of sample = 3).

Acknowledgements

This work was supported by the Materials for Enhanced Energy Technology program supported by a CREATE grant and discovery grant from the Natural Sciences and Engineering Research Council of Canada. The author would like to thank Dr. Elaine Humphrey for SEM images and EDS analysis in Advance Microscopy Facility at the University of Victoria and I would like to thank my colleague, Erik Pagan, for his help for schematic of Fig. 1.

Appendix A. Supplementary data

Supplementary data to this article can be found online at https://doi.org/10.1016/j.jpowsour.2018.09.076.

References

[1] M.F. Mathias, J. Roth, J. Fleming, W. Lehnert, Diffusion media materials and characterisation, Handb. Fuel Cells 3 (2003) 517–537.
[2] A. Bazylak, D. Sinton, Z.-S. Liu, N. Djilali, Effect of compression on liquid water transport and microstructure of PEMFC gas diffusion layers, J. Power Sources 163 (2007) 784–792.
[3] A. El-kharouf, T.J. Mason, D.J.L. Brett, B.G. Pollet, Ex-situ characterisation of gas diffusion layers for proton exchange membrane fuel cells, J. Power Sources 218 (2012) 393–404.
[4] S. Park, B.N. Popov, Effect of a GDL based on carbon paper or carbon cloth on PEM fuel cell performance, Fuel 90 (2011) 436–440.
[5] A. Forner-Cuenca, J. Biesdorf, L. Gubler, P.M. Kristiansen, T.J. Schmidt, P. Boillat, Engineered water highways in fuel cells: radiation grafting of gas diffusion layers, Adv. Mater. 27 (2015) 6317–6322.
[6] M.F. Mathias, J. Roth, J. Fleming, W. Lehnert, Diffusion media materials and characterisation, Handb. Fuel Cells 3 (2010) 517–537, https://doi.org/10.1002/9780470974001.f303046.
[7] J. Benziger, J. Nehlsen, D. Blackwell, T. Brennan, J. Itescu, Water flow in the gas diffusion layer of PEM fuel cells, J. Membr. Sci. 261 (2005) 98–106.
[8] S.G. Kandlikar, M.L. Garofalo, Z. Lu, Water management in a PEMFC: water transport mechanism and material degradation in gas diffusion layers, Fuel Cell. 11 (2011) 814–823.
[9] Z. Lu, M.M. Daino, C. Rath, S.G. Kandlikar, Water management studies in PEM fuel cells, part III: dynamic breakthrough and intermittent drainage characteristics from GDLs with and without MPLs, Int. J. Hydrogen Energy 35 (2010) 4222–4233.
[10] R. Flückiger, F. Marone, M. Stampanoni, A. Wokaun, F.N. Büchi, Investigation of liquid water in gas diffusion layers of polymer electrolyte fuel cells using X-ray tomographic microscopy, Electrochim. Acta 56 (2011) 2254–2262.
[11] S. Hasanpour, M. Hoorfar, A.B. Phillion, Characterization of transport phenomena in porous transport layers using X-ray microtomography, J. Power Sources 353 (2017) 221–229.
[12] A. Bazylak, Liquid water visualization in PEM fuel cells: a review, Int. J. Hydrogen Energy 34 (2009) 3845–3857.
[13] I.V. Zenyuk, D.Y. Parkinson, G. Hwang, A.Z. Weber, Probing water distribution in compressed fuel-cell gas-diffusion layers using X-ray computed tomography, Electrochem. Commun. 53 (2015) 24–28, https://doi.org/10.1016/j.elecom.2015.02.005.
[14] S. Prass, S. Hasanpour, P.K. Sow, A.B. Phillion, W. Mérida, Microscale X-ray tomographic investigation of the interfacial morphology between the catalyst and micro porous layers in proton exchange membrane fuel cells, J. Power Sources 319 (2016) 82–89.
[15] E.C.S. Transactions, T.E. Society, Fighting the Noise: towards the Limits of Subsecond X-ray Tomographic Microscopy of PEFC H. Xu vol. 80, (2017), pp. 395–402.
[16] S. Litster, D. Sinton, N. Djilali, Ex situ visualization of liquid water transport in PEM fuel cell gas diffusion layers, J. Power Sources 154 (2006) 95–105.
[17] K. Yoshizawa, K. Ikezoe, Y. Tasaki, D. Kramer, E.H. Lehmann, G.G. Scherer, Analysis of gas diffusion layer and flow-field design in a PEMFC using neutron radiography, J. Electrochem. Soc. 155 (2008) B223–B227.
[18] M. Ahadi, M. Tam, M.S. Saha, J. Stumper, M. Bahrami, Thermal conductivity of catalyst layer of polymer electrolyte membrane fuel cells: Part 1-Experimental study, J. Power Sources 354 (2017) 207–214.
[19] E. Sadeghi, N. Djilali, M. Bahrami, Effective thermal conductivity and thermal contact resistance of gas diffusion layers in proton exchange membrane fuel cells. Part 1: effect of compressive load, J. Power Sources 196 (2011) 246–254.
[20] M. Ahadi, M. Andisheh-Tadbir, M. Tam, M. Bahrami, An improved transient plane source method for measuring thermal conductivity of thin films: deconvoluting thermal contact resistance, Int. J. Heat Mass Tran. 96 (2016) 371–380.
[21] O. Burheim, P.J.S. Vie, J.G. Pharoah, S. Kjelstrup, Ex situ measurements of through-plane thermal conductivities in a polymer electrolyte fuel cell, J. Power Sources 195 (2010) 249–256.
[22] O.S. Burheim, J.G. Pharoah, H. Lampert, P.J.S. Vie, S. Kjelstrup, Through-plane thermal conductivity of PEMFC porous transport layers, J. Fuel Cell Sci. Technol. 8 (2011) 21013.
[23] O.S. Burheim, H. Su, S. Pasupathi, J.G. Pharoah, B.G. Pollet, Thermal conductivity and temperature profiles of the micro porous layers used for the polymer electrolyte membrane fuel cell, Int. J. Hydrogen Energy 38 (2013) 8437–8447.
[24] O.S. Burheim, G. Ellila, J.D. Fairweather, A. Labouriau, S. Kjelstrup, J.G. Pharoah, Ageing and thermal conductivity of porous transport layers used for PEM fuel cells, J. Power Sources 221 (2013) 356–365.
[25] O.S. Burheim, H. Su, H.H. Hauge, S. Pasupathi, B.G. Pollet, Study of thermal conductivity of PEM fuel cell catalyst layers, Int. J. Hydrogen Energy 39 (2014) 9397–9408.
[26] Z. Fishman, a. Bazylak, Heterogeneous through-plane porosity distributions for treated PEMFC GDLs. II. Effect of MPL cracks, J. Electrochem. Soc. 158 (2011) B846, https://doi.org/10.1149/1.3594636.
[27] M. Khandelwal, M.M. Mench, Direct measurement of through-plane thermal conductivity and contact resistance in fuel cell materials, J. Power Sources 161 (2006) 1106–1115.
[28] I. Nitta, T. Hottinen, O. Himanen, M. Mikkola, Inhomogeneous compression of PEMFC gas diffusion layer: part I, Experimental, J. Power Sources 171 (2007) 26–36.
[29] J. Becker, R. Flückiger, M. Reum, F.N. Büchi, F. Marone, M. Stampanoni, Determination of material properties of gas diffusion layers: experiments and simulations using phase contrast tomographic microscopy, J. Electrochem. Soc. 156 (2009) B1175–B1181.
[30] N. Zamel, X. Li, J. Shen, Numerical estimation of the effective electrical conductivity in carbon paper diffusion media, Appl. Energy 93 (2012) 39–44.
[31] M. Secanell, R. Songprakorp, A. Suleman, N. Djilali, Multi-objective optimization of a polymer electrolyte fuel cell membrane electrode assembly, Energy Environ. Sci. 1 (2008) 378, https://doi.org/10.1039/b804654a.
[32] M. Secanell, B. Carnes, A. Suleman, N. Djilali, Numerical optimization of proton exchange membrane fuel cell cathodes, Electrochim. Acta 52 (2007) 2668–2682, https://doi.org/10.1016/j.electacta.2006.09.049.